The VMC survey - XV. The Small Magellanic Cloud--Bridge connection history as traced by their star cluster populations

1
2
3
4
5
6
7
8
9
10
11
12
13
14
15
16
17
18
19
20
21
22
23
24
25
26
27
28
29
30
31
32
33
34
35
36
37
38
39
40
41
42
43
44
45
46
47
48
49
50
51
52
53
54
55
56
57
58
59
60

The VMC survey - XV. The Small Magellanic Cloud–Bridge connection history as traced by their star cluster populations[*]

Andrés E. Piatti[1,2]†, Richard de Grijs[3,4], Stefano Rubele[5], Maria-Rosa L. Cioni[6,7,8],
Vincenzo Ripepi[9] and Leandro Kerber[10]

[1] *Observatorio Astronómico, Universidad Nacional de Córdoba, Laprida 854, 5000, Córdoba, Argentina*
[2] *Consejo Nacional de Investigaciones Científicas y Técnicas, Av. Rivadavia 1917, C1033AAJ, Buenos Aires, Argentina*
[3] *Kavli Institute for Astronomy and Astrophysics, Peking University, Yi He Yuan Lu 5, Hai Dian District, Beijing 100871, China*
[4] *Department of Astronomy, Peking University, Yi He Yuan Lu 5, Hai Dian District, Beijing 100871, China*
[5] *INAF, Osservatorio Astronomico di Padova, vicolo dell'Osservatorio 5, I-35122 Padova, Italy*
[6] *Universität Potsdam, Institut für Physik und Astronomie, Karl-Liebknecht-Str. 24/25, 14476 Potsdam, Germany*
[7] *Leibniz-Institut für Astrophysik Potsdam, An der Sternwarte 16, 14482 Potsdam, Germany*
[8] *University of Hertfordshire, Physics, Astronomy and Mathematics, College Lane, Hatfield AL10 9AB, United Kingdom*
[9] *INAF-Osservatorio Astronomico di Capodimonte, Via Moiariello 16, 80131, Naples, Italy*
[10] *Universidade Estadual de Santa Cruz, Rodovia Ilhéus–Itabuna, km 16, 45662-200 Ilhéus, Bahia, Brazil*

21 January 2002

ABSTRACT

We present results based on YJK_s photometry of star clusters located in the outermost, eastern region of the Small Magellanic Cloud (SMC). We analysed a total of 51 catalogued clusters whose colour–magnitude diagrams (CMDs), having been cleaned from field-star contamination, were used to assess the clusters' reality and estimate ages of the genuine systems. Based on CMD analysis, 15 catalogued clusters were found to be possible non-genuine aggregates. We investigated the properties of 80% of the catalogued clusters in this part of the SMC by enlarging our sample with previously obtained cluster ages, adopting a homogeneous scale for all. Their spatial distribution suggests that the oldest clusters, $\log(t\ \mathrm{yr}^{-1}) \geqslant 9.6$, are in general located at greater distances to the galaxy's centre than their younger counterparts – $9.0 \leqslant \log(t\ \mathrm{yr}^{-1}) \leqslant 9.4$ – while two excesses of clusters are seen at $\log(t\ \mathrm{yr}^{-1}) \sim 9.2$ and $\log(t\ \mathrm{yr}^{-1}) \sim 9.7$. We found a trail of younger clusters which follow the Wing/Bridge components. This long spatial sequence does not only harbour very young clusters, $\log(t\ \mathrm{yr}^{-1}) \sim 7.3$, but it also hosts some of intermediate ages, $\log(t\ \mathrm{yr}^{-1}) \sim 9.1$. The derived cluster and field-star **formation frequencies as a function of age** are different. The most surprising feature is an observed excess of clusters with ages of $\log(t\ \mathrm{yr}^{-1}) < 9.0$, which could have been induced by interactions with the LMC.

Key words: techniques: photometric – galaxies: individual: SMC – Magellanic Clouds

1 INTRODUCTION

The near-infrared VISTA Survey of the Magellanic Clouds (VMC) system (Cioni et al. 2011) has been designed to obtain three epochs of data in the near-infrared passbands Y and J, and 12 epochs in the K_s, in order to reach a nominal survey depth of $Y = 21.9$, $J = 21.4$ and $K_s = 20.3$ mag (at a signal-to-noise ratio of 10) for individual tiles of ~ 1.5 deg^2

in size. The VMC survey covers a total area of ~ 170 deg^2, comprising the Large Magellanic Cloud (LMC), the Small Magellanic Cloud (SMC), the Magellanic Bridge and a few tiles covering the Magellanic Stream. Individual epochs have exposure times of 800 s (Y and J) and 750 s (K_s). The multi-epoch observations allow us to minimize variability effects in colours, particularly for bright objects, and guarantee homogeneous observing conditions among different passbands for a given epoch. Seeing constraints, imposed for the purpose of homogenizing crowded and uncrowded field observations, range between $1.0''$ and $1.3''$ (Y), $0.9''$ and $1.2''$ (J), and

1
2
3
4
5
6
7
8
9
10
11
12
13
14
15
16
17
18
19
20
21
22
23
24
25
26
27
28
29
30
31
32
33
34
35
36
37
38
39
40
41
42
43
44
45
46
47
48
49
50
51
52
53
54
55
56
57
58
59
60

2   *A. E. Piatti et al.*

$0.8''$ and $1.0''$ (K_s) and may exceed those values by 10% according to observing policy. The averaged K_s magnitudes resulting from the multi-epoch observations for RR Lyrae and Cepheid variable stars, with an accuracy of a few hundredths of a magnitude, will allow us to unveil the 3D structure of the Magellanic system (Ripepi et al. 2012; Moretti et al. 2014). On the other hand, stacking of these observations allows us to detect stars at the oldest main-sequence turn-off (MSTO) and derive the star-formation history (SFH) across the system with unprecedented quality (Rubele et al. 2012).

VMC data also allow us to perform a thorough study of the Magellanic Cloud (MC) star cluster population based on a homogeneous determination of star cluster parameters (Piatti et al. 2014). In addition, we can firmly establish whether the field star population has experienced the same or a similar SFH as the star cluster system. The addition of near-infrared photometry to existing optical photometry is aimed at disentangling the scatter that currently exists in the age–metallicity distribution (e.g. Piatti 2011b; Piatti & Geisler 2013), also enabling us to constrain extinction variations more precisely. Wide-field VMC data will produce a complete census of the cluster population that will be used to draw statistically robust conclusions about their differences between the Clouds. In addition, the search for new clusters based on stellar surface density distributions will work better in the Clouds than in the Galaxy because of the lower confusion along the line of sight.

The outermost, eastern region of the SMC and the associated onset of the Bridge are of significant scientific interest in the context of a putative scenario involving interactions between the MCs, which may be traced spatially and temporally. Indeed, the purpose of this paper is to present a photometric analysis of the catalogued clusters located in that region based on the most complete VMC data set to date. The available photometric data allow us to confirm the physical reality of the catalogued star clusters and (for the genuine clusters) estimate their fundamental parameters. We also investigate the cluster frequency in the region of interest to assess whether star clusters and field stars have evolved as a coupled system.

This paper is organised as follows. The VMC data collection and reduction is presented in Section 2, while the cluster sample is described in Section 3. Sections 4 and 5 deal with the cleaning procedure pertaining to the clusters' colour–magnitude diagrams and the astrophysical property estimates for the clusters, respectively. In Section 6 we discuss the photometric results, derive the cluster frequency and compare it to the field star formation history. We summarize our conclusions in Section 7.

2   VMC DATA COLLECTION AND REDUCTION

The VMC survey (Cioni et al. 2011) has collected more than half of the observations scheduled as part of a global observing campaign with the VISTA telescope, where observations for five other ESO public surveys are also carried out in service mode (Arnaboldi et al. 2013). The survey's SMC and Magellanic Bridge areas will eventually cover 42 deg^2 and 21 deg^2 (27 and 13 VISTA tiles), respectively. One tile covers uniformly an area of ~ 1.5 deg^2, representing a mosaic

of six paw-print images in a given passband (YJK_s). Figure 1 shows the distribution of the VMC tiles superimposed on that of the star clusters (dots) catalogued by Bica et al. (2008, hereinafter B08) in the SMC and the western Bridge regions. On the other hand, viewing the SMC as a triaxial galaxy (and adopting the declination, Dec, right ascension, RA, and line-of-sight as the three axes), Crowl et al. (2001) found axial ratios of approximately 1:2:4. Based on this result, and to describe the clusters' spatial distribution, Piatti et al. (2007a) used an elliptical rather than a spherical framework so as to reflect more meaningfully the flattening of the galaxy. This reference system – with one of its axes parallel to the SMC Bar and the other perpendicular to that direction – seems more appropriate to describe the clusters' age and metallicity distributions than one with axes along the right ascension and declination directions (see, e.g., Piatti et al. 2008; Piatti 2011b, 2012b). Two ellipses with semimajor axes of $2.4°$ and $6.0°$ are also shown. The ellipses are centred at RA = 00h 52m 45s, Dec = $-72°$ $49'$ $43''$ (J2000) (Crowl et al. 2001) and have axis ratios, $b/a = 1/2$. Thus the clusters' spatial distribution correlates better with a pseudo-elliptical (projected) distance coordinate measured from the galactic centre than with the radial distance, or with distances defined along the right ascension or declination axes.

The VMC data are processed with the VISTA Data Flow System pipeline, version 1.3 (VDFS Irwin et al. 2004), and calibrated to match the VISTA photometric system, which is close to the Vegamag system. We extracted the observational data from the VISTA Science Archive (VSA, Cross et al. 2012). The processed paw-print images were used to derive the effective point-spread functions (PSFs) using the IRAF[1]/DAOPHOT routines (Stetson, Davis & Crabtree 1990). We generated a reference PSF, which was convolved with the paw-print images to homogenize the resulting PSFs. We repeated these steps for each epoch separately. Finally, all homogenised paw-print images were combined using the SWARP tool (Bertin et al. 2002), as described in Rubele et al. (2012), thus generating deep tile images with homogeneous PSFs.

We performed PSF photometry on the homogenized, deep tile images of VMC tiles SMC 3_5, 4_5, 5_6, 6_5 and BRI 2_3. We focussed on these tiles because they are among the first fully or mostly completed tiles in the eastern region of the SMC (see column 4 of Table 1). Figure 1 shows that they extend over a vast region on the outermost, eastern side of the SMC and the associated onset of the Bridge, where early galactic stellar populations and those recently formed are supposed to co-exist as witnesses of the galaxy's formation and its tidal interaction with the Large Magellanic Cloud (LMC). Note that these tiles include, statistically speaking, an important percentage of the star clusters catalogued in that region, thus allowing us to draw robust conclusions about their star-formation history. The PSF model was created using ~ 2500 stars which were uniformly distributed and had magnitudes close to the saturation limit + 1.5 mag (for the VMC survey, the single paw-print saturation lim-

---

its are $Y = 12.9$ mag, $J = 12.7$ mag and $K_s = 11.4$ mag). Subsequently, we used the ALLSTAR routine to perform the final PSF photometry on the deep tile images in all three filters and correlated the resulting tables, adopting a tolerance of one arcsec. We applied aperture corrections using catalogues retrieved from the VSA[2] (Lewis, Irwin & Bunclark 2010; Cross et al. 2012) for the bulk of the observed stars.

We performed a large number of artificial-star tests to estimate the incompleteness and error distribution of our data for each deep tile image. For each VMC tile we generated $\sim 20 \times 10^6$ artificial stars following the steps outlined in Rubele et al. (2012). We used a spatial grid of 25 pixels in width and with a spatial magnitude distribution proportional to the square of the magnitude. This latter choice allowed us to better map the completeness and error levels in the less complete regions of the colour–magnitude diagram (CMD). Table 1 lists the magnitudes of stars with photometric errors of less than 0.10 mag ($mag_{0.1}$) and the magnitudes representing the 50% completeness level. Our previous experience (Cioni et al. 2011; Rubele et al. 2012; Li et al. 2014) taught us that the widest colour range, i.e., the $Y - K_s$ colour, is optimal for cluster studies, because it makes it easier to distinguish different cluster main sequences (MSs), particularly their turn-off (TO) regions, and the red-giant phases. This colour is also characterized by a higher sensitivity to reddening and metallicity than either the $Y - J$ or $J - K_s$ colours. Consequently, the subsequent analysis is mainly based on the K_s versus $Y - K_s$ CMDs; the J versus $Y - J$ and K_s versus $J - K_s$ CMDs **have been constructed and used to confirm the isochrones matched in the K_s versus $Y - K_s$ CMDs.**

3 THE CLUSTER SAMPLE

We delimited the outermost eastern region of the SMC and the associated onset of the Bridge by an ellipse with a semimajor axis of $2.4°$ and relative RA coordinates $\geqslant 1.7°$ (see Fig. 1). The star cluster population in that region comprises 79 objects according to the B08 catalogue; 27 (34%) have been studied in previous photometric studies (see, e.g., Glatt, Grebel & Koch 2010; Piatti et al. 2011). Fifty-one out of the 79 catalogued clusters are spread across the VMC tiles considered here, which added to 12 other previously studied clusters located outside these VMC tile areas, results in a more significant cluster sample (80%) than that previously studied. Note that the 51 clusters on the VMC tiles do not only represent a larger percentage of the cluster population in that region (65%) with respect to the previously studied clusters, but here we also analyse them in a homogeneous manner, thus enabling us to trace their formation history spatially. To date, the catalogue of B08 is the most complete compilation of star clusters in the SMC covering the extension of both Clouds and the Bridge. Particularly, because of the lower surface brightness of the background and the less-populous nature of the outer SMC regions and the Bridge, star clusters stand out more, and incompleteness effects are expected to be less important than in the inner regions of the Clouds.

Recognising catalogued star clusters in deep VMC tile images is neither straighforward nor simple. On the one hand, the catalogued objects were originally identified from optical images (e.g., from the Digitized Sky Survey, DSS[3], images) which sometimes look rather different compared with their appearance at near-infrared wavelengths. In addition, the spatial resolution and depth of the images on which the clusters were identified differ from the equivalent parameters pertaining to the VMC images. Thus, for instance, single relatively bright stars might look like an unresolved compact cluster in images of lower spatial resolution, or unresolved background galaxies could be mistaken for small star clusters in shallower images. Offsets in the coordinates compiled by B08 with respect to the objects' centres cannot be ruled out either.

To avoid mismatches between observed objects and the actual list of catalogued clusters, we first overplotted the positions of the catalogued clusters (B08) on the deepest K_s image. This way, based on using the coordinates provided by B08, we visually recognized the observed clusters one by one in the K_s image. Next, we searched for these clusters in the DSS and downloaded $15' \times 15'$ B images centred on the coordinates resolved by the SIMBAD[4] astronomical data base and compared them with equivalent cut-outs derived from the K_s VMC survey. Thus, we correctly recognized the clusters in both the optical and near-infrared regimes. Note that the main aim of this task is to confirm the cluster coordinates and sizes, in order to extract from the tile-image PSF photometry the magnitudes of the stars in the cluster region. We are not interested in properties such as the clusters' structure, stellar density profiles or radii, but in the stars which allow us to meaningfully define the clusters' fiducial sequences in their CMDs. Table 2 lists the complete cluster sample, as well as the coordinates and radii adopted for extracting the stellar PSF photometry; the cluster's radius was taken either from a visual inspection of the deepest K_s image (where the profile disappears into the background noise), from B08 or from both sources combined. The observed objects are of small angular size, typically $\sim 0.7'$ in diameter (~ 12.2 pc).

4 CLEANING THE CLUSTER CMDS

In general, the extracted cluster CMDs represent the composite stellar populations distributed along the respective lines of sight. Since they account for the luminosity function, colour distribution and stellar density towards a given region on the sky, CMD analysis alone might lead to an incorrect interpretation. On the other hand, the CMDs of the stars located within a region around the catalogued cluster centres are a helpful tool to assess the reality of the density enhancements. They may imply that we are dealing with

---

[2] http://horus.roe.ac.uk/vsa/

[3] The Digitized Sky Surveys were produced at the Space Telescope Science Institute under U.S. Government grant NAG W-2166. The images of these surveys are based on photographic data obtained using the Oschin Schmidt Telescope on Palomar Mountain and the UK Schmidt Telescope. The plates were processed into the present, compressed digital form with the permission of these institutions.

[4] http://simbad.u-strasbg.fr/simbad/

4   A. E. Piatti et al.

the presence of a genuine star cluster, a chance grouping of stars along the line of sight or a non-uniform distribution of interstellar material in the region of interest. Note that catalogued cluster candidates appear on the sky as small concentrations of stars, although this does not necessarily imply that such concentrations constitute real, physically bound systems.

For these reasons, we first statistically constructed CMDs representing the field along the line of sight towards the individual clusters, which we then used to clean the cluster CMDs. We employed the cleaning procedure developed by Piatti & Bica (2012, see their fig. 12). The method compares the extracted cluster CMD to four distinct CMDs composed of stars located reasonably far from the object, but not too far so as to risk losing the local field-star signature in terms of stellar density, luminosity function and/or colour distribution. The four field regions were designed to cover an equal area as that of the cluster (a circular area of three times the cluster radius), and they were placed to the north, east, south and west of the cluster area. Note that large areas were chosen to increase the statistics and hence the reliability of the cleaning process.

Comparisons of field and cluster CMDs have long been done by comparing the numbers of stars counted in boxes distributed in a similar manner throughout both CMDs. However, since some parts of the CMD are more densely populated than others, counting the numbers of stars within boxes of a fixed size is not universally efficient. For instance, to deal with stochastic effects at relatively bright magnitudes (e.g., fluctuations in the numbers of bright stars), larger boxes are required, while populous CMD regions can be characterized using smaller boxes. Thus, use of boxes of different sizes distributed in the same manner throughout both CMDs leads to a more meaningful comparison of the numbers of stars in different CMD regions. By starting with reasonably large boxes – $(\Delta K_s, \Delta(Y - K_s)) = (1.00,\ 0.25)$ mag – centred on each star in the four field CMDs and by subsequently reducing their sizes until they reach the stars closest in magnitude and colour, separately, we defined boxes which result in use of larger areas in field CMD regions containing a small number of stars, and vice versa (see Fig. 2, top right-hand panel, where we used an annulus -outer and inner radii equal to 3.163 and 3.0 times the cluster radius- around the cluster instead of one of the four selected circular areas for illustrative purposes). Next, we plotted all these boxes for each field CMD on the cluster CMD and subtracted the star located closest to each box centre.

Since we repeated this task for each of the four field-CMD box samples, we could assign a membership probability to each star in the cluster CMD. This was done by counting the number of times a star remained unsubtracted in the four cleaned cluster CMDs and by subsequently dividing this number by four. Thus, we distinguished field populations projected onto the cluster area, i.e., those stars with a probability $P \leqslant 25\%$, stars that could equally likely be associated with either the field or the object of interest ($P = 50\%$), and stars that are predominantly found in the cleaned cluster CMDs ($P \geqslant 75\%$) rather than in the field-star CMDs. Figure 2 illustrates the performance of the cleaning procedure for the HW77 field, where we plotted three different CMDs: that for the stars located within the cluster radius (top left-hand panel), a single-field CMD for an annulus -outer and inner radii equal to 3.163 and 3.0 times the cluster radius-centred on the cluster, as well as the cleaned cluster CMD (bottom left-hand panel). The schematic diagram with a superimposed circle of radius equal to the cluster radius is shown in the bottom right-hand panel. The pink, light and dark blue solid circles in the bottom panels represent stars with $P \leqslant 25\%$, $P = 50\%$ and $P \geqslant 75\%$, respectively. Note that when comparing observed cluster and field CMDs **for the HW 77 region** (top left- and right-hand panels), the cluster region contains brighter red clump (RC) stars and a younger MSTO : $K_s(\mathrm{RC_{HW77}}) \sim 17.0$ mag, $K_s(\mathrm{RC_{field}}) \sim 17.5$ mag, $K_s(\mathrm{MSTO_{HW77}}) \sim 19.5$ mag and $K_s(\mathrm{MSTO_{field}}) \sim 20.5$ mag, which suggests that HW77 is projected against a relatively older composite stellar population. A full set of figures for the remaining objects studied here is provided in the online version of the journal.

To assess whether a catalogued cluster is a genuine aggregate, we inspected both the cluster's schematic diagram and the cleaned CMD. Objects showing some apparent concentration in the sky of stars with $P \geqslant 75\%$ that do not define clear cluster sequences in the cleaned CMDs were assumed to be possible non-genuine aggregates. We found that nearly 30% (15 catalogued clusters) of our cluster sample fall into this latter category. This relatively high percentage compares well with recent results of different cluster sample analyses in both Magellanic Clouds, which suggest that the B08 cluster catalogue might contain between 10% and 30% of possible non-genuine aggregates (Piatti & Bica 2012; Piatti 2014a; Piatti et al. 2014). Likewise, we found two clusters (GKH22 and GKH24) that could not be resolved by our photometry and another (BS226) that could not be recognized in any image using the coordinates given by B08. The relevant information about the status of these objects is provided in the final column of Table 2.

5   FUNDAMENTAL CLUSTER PARAMETERS

We used the cleaned cluster CMDs to estimate the fundamental cluster parameters by matching the observations with the theoretical isochrones of Bressan et al. (2012). In performing this task, one has to deal with parameters such as the reddening, distance, age and metallicity. Our strategy consisted of obtaining the reddening values from an independent source, assuming the mean SMC distance modulus for all clusters and adopting for the cluster ages the ages of the isochrones which best reproduced their CMD features. We started with isochrones for a metallicity of $Z = 0.003$ ([Fe/H] $= -0.7$ dex), which corresponds to the mean SMC cluster metal content during the last ~ 2–3 Gyr (Piatti & Geisler 2013), and employed isochrones for other metallicities as required. Note that the difference in $Y - K_s$ colour between isochrones for $Z = 0.003$ and 0.001 ([Fe/H]$= -1.1$ dex) is ~ 0.1 mag in the MSTO region, ~ 0.05 mag at the subgiant branch (SGB) and ~ 0.15 mag at the tip of the red-giant branch for ages between $\log(t\ \mathrm{yr}^{-1}) = 9.3$ (2 Gyr) and $\log(t\ \mathrm{yr}^{-1}) = 9.6$ (4.0 Gyr). This difference is ~ 0.05 mag smaller for $\log(t\ \mathrm{yr}^{-1}) = 9.8$ (6.3 Gyr). This small difference suggests that the $Y - K_s$ colour is not sensitive to metallicity differences smaller than Δ[Fe/H]$=0.4$ dex if we keep in mind the relatively sparse nature of the majority of our clusters and the intrinsic spread of the stars in the

CMDs. Indeed, we tried using isochrones with metallicities [Fe/H] = -0.5 and -0.9 dex and found negligible differences with respect to that of [Fe/H] = -0.7 dex. Nevertheless, only four clusters in our sample (L109, L110, B168 and HW85) appeared older than $\log(t \text{ yr}^{-1}) = 9.3$, and we carefully paid attention to the effects of metallicity differences.

According to Dutra et al. (2001), the SMC is optically thin, characterized by average foreground and internal $E(B-V)$ colour excesses of 0.05±0.05 mag and 0.04 mag (computed from a reddening for the SMC surroundings of $E(B-V) = 0.02\pm0.02$ mag), respectively. We took advantage of the Magellanic Cloud extinction values based on RC stellar photometry provided by the OGLE III collaboration (Udalski 2003), as described in Haschke, Grebel & Duffau (2011), to estimate $E(B-V)_{OGLE\,III}$ colour excesses for 18 clusters in our sample which are located in the area covered by OGLE III. Likewise, we made use of the NASA/IPAC Extragalactic Data base[5] (NED) to infer Galactic foreground reddening values, $E(B-V)_{NED}$, for the same cluster list. Next, we computed the difference, $\Delta E(B-V) = E(B-V)_{OGLE\,III} - E(B-V)_{NED} = 0.025 \pm 0.005$ mag, in good agreement with the mean internal reddening given by Dutra et al. (2001). Note that this mean SMC internal reddening renders the isochrones 0.02 mag redder in $Y-K_s$ and 0.01 mag fainter in K_s, respectively, in the cleaned cluster CMDs. In matching isochrones, we started by adopting either $E(B-V)_{OGLE\,III}$ values or $E(B-V)_{NED} + 0.03$ mag, combined with the equations $E(Y-K_s) = 0.84 \times E(B-V)$ and $K_s = M_{K_s} + (m-M)_0 + 0.372 \times E(B-V)$, assuming $R_V = 3.1$ (Cardelli, Clayton & Mathis 1989; Gao et al. 2013). The final $E(B-V)$ values are listed in Table 2. We found two clusters which may be affected by differential reddening, i.e., HW74 (Bratsolis, Kontizas & Bellas-Velidis 2004) and HW81 (embedded in an HII region Testor et al. 2010). Two other clusters (BS189, BS190) are characterized by noticeably large $E(B-V)$ values, that may also be influenced by differential reddening. In particular, BS189 is by far the most reddened cluster known in the Magellanic Clouds; it is even more heavily reddened than any cluster in the highly reddened LMC/30 Doradus region (Tatton et al. 2013).

For all clusters, we adopted the mean SMC distance modulus $(m-M)_0 = 18.90 \pm 0.10$ mag ($60.0^{+3.0}_{-2.5}$ kpc) (Glatt, Grebel & Koch 2010) and an average line-of-sight SMC disc depth of 6 kpc (Crowl et al. 2001). Bearing in mind that any cluster in the present sample could be placed in front of or behind the SMC, we conclude that the difference in apparent distance moduli could be as large as $\Delta(K_s - M_{K_s}) \sim 0.2$ mag. This difference is much smaller than the difference between two closely spaced isochrones as used here ($\Delta \log(t \text{ yr}^{-1} = 0.1, \Delta M_{K_s} \sim 0.4$ mag), so that adoption of a unique value for the distance modulus does not dominate the final error budget incurred in matching isochrones to the cluster CMDs.

In the matching procedure, we used subsets of isochrones ranging from $\Delta \log(t \text{ yr}^{-1}) = -0.3$ to $+0.3$, straddling the initial rough age estimates. Since the Bressan et al.

(2012) isochrones are defined in the Vegamag system (where Vega has a magnitude of zero in all filters, by definition), we subtracted 0.074 mag in Y and 0.003 mag in K_s from the isochrones before matching them to the cluster CMDs (Rubele et al. 2015). Thus, we worked with both theoretical models and observed CMDs which were defined in the VISTA system. We found that isochrones bracketing the derived mean age by $\Delta \log(t \text{ yr}^{-1}) = \pm0.1$ represent the overall age uncertainties owing to the observed dispersion in the cluster CMDs. Although in some cases the age dispersion is smaller than $\Delta \log(t \text{ yr}^{-1}) = 0.1$, we prefer to keep the former value as an upper limit to our error budget (Piatti et al. 2011; Piatti 2014b; Piatti et al. 2014, among others). Finally, we adopted for the cluster age/metallicity those values corresponding to the isochrone which best reproduced the cluster's main features in the CMD. Table 2 lists the resulting age and metallicity values for 33 of the confirmed clusters, while the bottom left-hand panel of Fig. 2 illustrates our isochrone-matching procedure in the context of the CMD of HW77.

Fourteen clusters have previous age estimates based on matching of theoretical isochrones to their CMDs. We previously studied seven of these based on Washington CT_1 photometry and the remaining clusters were analysed by Glatt, Grebel & Koch (2010) as part of the Magellanic Cloud Photometric Surveys (MCPS Zaritsky et al. 2002). We took advantage of the availability of the Washington data to perform a sound comparison of the ages resulting from both the Washington photometry and the present results. First, we cleaned the cluster CMDs following the precepts described in Section 4. Then, we adopted the mean SMC distance modulus, $E(B-V)$ colour excesses and metallicities discussed above. Finally, we matched isochrones to the cluster CMDs, shifted by $E(C-T_1) = 1.97E(B-V)$ and $T_1 = M_{T_1} + 2.62E(B-V) + (m-M)_0$ (Geisler & Sarajedini 1999). The resulting ages are listed in the final column of Table 2. When comparing these values with the VMC cluster ages, we found a difference of $\Delta \log(t \text{ yr}^{-1}) = -0.05\pm0.10$, with the VMC ages being slighlty older. On the other hand, a direct comparison of the age estimates derived by Glatt, Grebel & Koch (2010) (see the final column of Table 2) and our values shows that our ages are $\Delta \log(t \text{ yr}^{-1}) = 0.5 \pm 0.5$ older. We recall that Glatt et al. did not perform any decontamination of field stars from the cluster CMDs and they therefore had to decide whether to include luminous supergiants in their fits, since the apparent MSTO of sparse, young clusters is subject to pronounced statistical fluctuations. It is possible that the lack of cleaned CMDs and their shallower photometry did not allow them to achieve more reliable age estimates.

6 ANALYSIS

In this section we address the cluster-formation history on the outermost, eastern side of the SMC and the connected onset of the Bridge by analysing the spatial dependence of their age distribution. We first enlarged the cluster sample by adding previously studied objects located in this region but beyond the VMC tile areas. We found a total of 12 clusters with available CT_1 Washington photometry and ages estimated from the matching of isochrones to their CMDs.

6   A. E. Piatti et al.

As shown above, these age estimates are in very good agreement with those of the VMC clusters. We needed to correct the $CT1_1$-based ages by only $\Delta \log(t \text{ yr}^{-1}) = -0.05$ to establish a homogeneous age scale, i.e., that of the present VMC cluster ages. The properties of the additional cluster sample are listed in Table 3.

The enlarged cluster sample is shown in Fig. 3 using solid circles. We used a colour scale to distinguish among clusters with different $\log(t \text{ yr}^{-1})$ values, so that darker colours correspond to older clusters. The spatial distribution of the clusters seems to suggest that while the 8 oldest clusters – $\log(t \text{ yr}^{-1}) \geqslant 9.6$ (see Tables 2 and 3) – are in general located at greater distances to the galaxy's centre than the younger clusters – $9.0 \leqslant \log(t \text{ yr}^{-1}) \leqslant 9.4$ – there is also a trail of young clusters, $\log(t \text{ yr}^{-1}) < 8.4$, along the onset of the Bridge. Since we are dealing with 80% of the catalogued clusters in this part of the SMC – the remaining 20% are mostly located in the Bridge – our results can be considered as based on an unbiased cluster sample.

Viewing the SMC as a triaxial galaxy with the Dec, RA and line of sight as the three axes, Crowl et al. (2001) found axial ratios of approximately 1:2:4. Based on this result, and aiming at estimating the clusters' projected distances to the SMC's centre, we adopted the elliptical framework described in Section 2, where a is the semimajor axis of an ellipse centred on the SMC centre, for a b/a axis ratio of $1/2$ and one point of its trajectory coinciding with the position of the cluster of interest. For our sample clusters with $\log(t \text{ yr}^{-1}) \geqslant 9.6$ we obtained $a = (6.0 \pm 1.3)°$, in excellent agreement with the mean value for the 16 known SMC clusters spanning the same age range (Dolphin et al. 2001; Piatti 2011a; Da Costa & Hatzidimitriou 1998; Mighell, Sarajedini & French 1998; Piatti et al. 2007c; Piatti 2012a). Note that both the present cluster sample and the handful of the oldest known clusters span a semimajor axis range between $\sim$ 2° and 9°; the latter are found at any position angle. For clusters with $9.0 \leqslant \log(t \text{ yr}^{-1}) \leqslant 9.4$, we obtained $a = (4.9 \pm 1.8)°$. Although the latter result is statistically indistinguishable from that for the oldest clusters in the sample, the smaller mean value suggests that the intermediate-age clusters are spatially slightly more concentrated than the older cluster population. This trend is in agreement with Carrera et al. (2008), Piatti (2012b,a) and Cignoni et al. (2013), who showed that SMC clusters and field stars follow a similar trend in the sense that the larger the semimajor axis is, the older their ages are, with a non-negligible dispersion.

The other interesting feature of Fig. 3 is the trail of younger clusters that seems to follow the Wing/Bridge components. Such a long spatial sequence, which seems to originate directly in the inner SMC disc, does not only harbour very young clusters, $\log(t \text{ yr}^{-1}) \sim 7.3$, but also some of intermediate ages, $\log(t \text{ yr}^{-1}) \sim 9.1$. McCumber, Garnett & Dufour (2005) imaged a star field located in the Wing with the *Hubble Space Telescope (HST)*'s WFPC2 camera and also found a wide age range, i.e., $\log(t \text{ yr}^{-1}) \sim 8.0$–9.2, while Sabbi et al. (2009) used the *HST*/ACS camera to observe two fields in the Wing. They found evidence of enhancement in the star-formation activity starting from $\log(t \text{ yr}^{-1}) \sim 8.7$. Continuous star-formation activity at intermediate ages, as well as a very recent star-formation phase, have recently been found by Ripepi et al. (2014) and Skowron et al. (2014). In addition, Bagheri, Cioni & Napiwotzki (2013)

and Noël et al. (2013) showed evidence of the presence of intermediate-age stars that could have been stripped from the SMC, which has also been predicted by models of gas replenishment from the SMC to the LMC (Bekki & Chiba 2007). Harris (2007) did not detect intermediate-age stellar populations associated with the Bridge, which led him to conclude that the material which was stripped from the SMC to form the Bridge may have consisted of very nearly pure gas. However, the present cluster ages agree well with results from field-star studies which showed that the Bridge does not only contain gas from which new generations of stars might be formed but also older stellar populations. Whether (i) this star-formation process took place along the Wing/Bridge components, (ii) clusters/field stars were stripped from the SMC in the direction of the LMC and (iii) their formation history is a continuous or a burst-like chain of events are questions that are still being debated and which deserve further investigation. From the perspective of the clusters' ages, the Wing/Bridge structures seem to have existed at least during the past 1–2 Gyr, i.e., $\log(t \text{ yr}^{-1}) \sim$ 9.0–9.3.

Figure 4 shows a time series pertaining to the clusters' spatial distribution in intervals of $\Delta\log(t \text{ yr}^{-1}) = 0.2$; the lower limit included in the interval. We have drawn, in every panel, all catalogued clusters (dots) and the same two ellipses as in Fig. 3. The present cluster sample (Tables 2 and 3) is shown as solid circles. Figure 4 reveals that the ages of the clusters in the outermost, eastern part of the SMC cover the entire age range, with the exception of the oldest ages and the interval $7.4 \leqslant \log(t \text{ yr}^{-1}) < 7.8$. The lack of SMC clusters that are as old as the Galactic globular clusters has long been known (Glatt et al. 2008). On the other hand, the absence of clusters in the younger age range indicated can be linked to the minimum age found by Glatt, Grebel & Koch (2010), $\log(t \text{ yr}^{-1}) \sim 7.5$, based on an age distribution composed of 821 clusters and associations distributed across the main body of the galaxy; only ages with $\Delta\log(t \text{ yr}^{-1}) < 0.5$ were used.

Clusters older than $\log(t \text{ yr}^{-1}) \sim 9.2$ appear to be found predominantly in the outer disc, whereas younger clusters tend to be mostly located along the Wing/Bridge interface. Two peaks populated by older clusters are seen at $\log(t \text{ yr}^{-1}) \sim 9.0$–9.4 and $\log(t \text{ yr}^{-1}) \sim 9.6$–9.8, in very good agreement with enhanced episodes of cluster formation that occurred throughout the galaxy Piatti (2011b, and reference therein). Both peaks were found by Noël et al. (2009) from the recovery of the formation history of stars observed in 12 fields in the B, R bands with the 100 inch telescope at Las Campanas Observatory. Harris & Zaritsky (2004) also detected the younger peak based on their MCPS data, whereas Rezaei kh. et al. (2014) showed the presence of the older peak based on observations of long-period variable stars.

6.1   Star cluster frequency

We constructed the star cluster **formation frequency as a function of age** (CF) – the number of clusters per unit time interval as a function of age – to compare it with that derived under the assumption that they are characterized by a similar formation history as that of the field stars projected along their respective lines of sight. We were interested in obtaining the CFs for clusters located in tiles SMC 3_5, 4_5,

5_6 and 6_5 for which Rubele et al. (2015) obtained star-formation rates using the same VMC photometric data set.

The first step in generating the CF consisted of considering the age errors. Indeed, by taking into account such errors, the interpretation of the resulting CF can differ appreciably from that obtained using only the measured ages without accounting for their uncertainties. However, treatment of the age errors in the CF is not straightforward. Moreover, even if errors did not play an important role, binning of the age ranges could also bias the results. At first glance, a fixed age-bin size may not be appropriate, since the resulting age distribution depends on the adopted age interval, and the age errors are typically a strong function of age. On the contrary, adoption of age-bin widths on the order of the clusters' age errors in the interval of interest appears more meaningful. This would lead to the selection of narrow bins (in linear age) for young clusters and relatively broader age bins at older ages (Piatti & Geisler 2013; Piatti 2014a). To account for the effects of the age uncertainties in the CF while taking into account that any individual point in the CF may fall either in the respective age bin or in any of the adjacent bins, we followed Piatti (2014b).

For our purposes, we first considered the cluster age range, split into bins of $\Delta \log(t \text{ yr}^{-1}) = 0.10$. On the other hand, each age data point and its associated uncertainty ($\sigma(t)$) covers a segment with a size of $2 \times \sigma(t)$ (which may or may not fall fully in one of the age bins) and has dimensions smaller, similar to or larger than the age bin in which it is found. For this reason, we weighted the contribution of each age data point to each of the associated age bins, with the sum total of all weights being equal to unity. The assigned weight was computed as the fraction of the age segment that falls within the relevant age bin. In practice, for each age interval we looked for clusters with ages that fall inside the age bin considered, as well as clusters where $t \pm \sigma(t)$ could cause them to fall in the same age bin. Note that if $t \pm \sigma(t)$ causes a cluster's age range to extend beyond the main age bin considered (e.g., from one bin to the next), then we consider that that cluster may have an age that also places it inside the extended age interval considered. Figure 5 shows the resulting CF (thick solid line). This CF has been normalized to the total number of clusters. Note the discontinuity at $\log(t \text{ yr}^{-1}) = 7.4$–7.8, which may be owing to the small number of clusters in our sample. The younger part of the CF is mainly based on clusters located in the inner tiles, SMC 3_5 and 4_5, while the remaining outer tiles (5_6 and SMC 6_5) mostly contribute to the older regime.

To place the CF resulting from our small cluster sample in the overall context of the SMC's cluster population, we also included the CF constructed on the basis of the cluster age determinations of de Grijs & Goodwin (2008; thick dashed line). The latter authors obtained best-fitting ages for more than 300 SMC clusters based on broad-band photometric measurements at optical wavelengths. They validated their resulting age estimates with respect to both those obtained by other teams using similar approaches and by reference to their extensive validation of the modelling approach used. Despite the differences in both cluster numbers and photometric completeness limits between both studies, the overall trends seen in Fig. 5 are similar.

The effects of small-number statistics are apparent in the stochastic fluctuations in the CF based on the VMC data set. The main difference between the CF constructed based on the VMC data set with respect to that resulting from the de Grijs & Goodwin (2008) data is the relatively larger number of older clusters in the VMC data. A careful comparison between both data sets reveals that the completeness limit in terms of cluster masses of the VMC data sets in at much lower masses than that pertaining to the broad-band data set. The older, lower-mass clusters seen in the near-infrared VMC data had already faded to below the detection limit in the bluest filter used by de Grijs & Anders (2008). All other apparent differences between both observational CFs can be traced back to small-number statistics. Note that the similarity between both CFs, which are nevertheless based on very different lower-mass limits, implies indirectly that the cluster mass function in the SMC is well represented by a power-law function down to the lowest accessible masses (cf. de Grijs & Goodwin 2008).

Finally, we compare the present, VMC-based CF to that obtained from the star-formation rates derived by Rubele et al. (2015) from the same VMC tiles and PSF photometry data set used here. They subdivided each tile into 12 subregions of $21.0' \times 21.5'$ ($\sim 0.12 \text{ deg}^2$) and derived their star-formation histories as described in detail in Rubele et al. (2012). Briefly, for a range of distance moduli and visual extinction estimates, 'partial models' are derived for the entire range of metallicities and ages of relevance. Partial models are synthetic stellar populations, each covering small bins in age and metallicity, shifted to the desired distance and extinction. Each partial model is 'degraded' to the conditions of the actual observations by convolving them with the distributions of photometric errors and completeness. The linear combination of partial models that optimally matches the observed Hess diagrams is found by means of the StarFISH optimisation code (Harris & Zaritsky 2001). The coefficients of this linear combination of partial models (including the best-fitting distance modulus and extinction) are directly converted into the star-formation rates.

We assumed that clusters are formed with a power-law mass distribution characterized by a slope of $\alpha = -2$ (Baumgardt et al. 2013; Piatti 2014b) and with a rate that is proportional to the field-star formation rate determined by Rubele et al. (2015) for the individual subfields pertaining to our clusters, taking into account the corresponding uncertainties. We used cluster masses from $\log(M_{cl} [\text{M}_\odot]) = 2.2$ to $\log(M_{cl} [\text{M}_\odot]) = 5.0$ (de Grijs & Goodwin 2008; Glatt et al. 2011) and normalized the resulting CF by the total number of clusters used, so that it can be compared directly to the observed distribution. Figure 5 shows the resulting model CF, where the uncertainties are indicated using thin solid lines. As can be seen, the observed and modeled CFs are different. For ages in excess of $\log(t \text{ yr}^{-1}) \sim 9.4$ the model CF is higher than the observed frequency, possibly because we did not take into account any cluster dissolution. According to Lada & Lada (2003), most – if not all – stars form in some sort of cluster. This implies that field stars are the result of cluster dissolution and do not originate from an independent formation mechanism, so that the difference between the observed and modeled CFs would then be the result of the prevailing cluster dissolution rate.

The decrease of the star-formation activity that started at $\log(t \text{ yr}^{-1}) \sim 9.0$ and was interrupted by a burst-like formation event which occurred at $\log(t \text{ yr}^{-1}) \sim 8.5$ was also

8   *A. E. Piatti et al.*

documented by Harris & Zaritsky (2004), Noël et al. (2009), Sabbi et al. (2009) and Rubele et al. (2015). However, the observed CF is significantly higher for ages younger than $\log(t \text{ yr}^{-1}) \sim 9.0$. Even though the model CF requires additional refinements, the clear cluster excess deserves further analysis. If we now keep in mind de Grijs, Goodwin & Anders (2013)'s results, who showed that there is no evidence of significant destruction other than that expected from stellar dynamics and evolution for simple stellar population models for ages up to 1 Gyr – $\log(t \text{ yr}^{-1}) = 9$ – we speculate that such a cluster excess could be evidence of enhanced cluster formation in this part of the SMC with respect to that on the western side. Indeed, the number of clusters on that latter side is significantly smaller (see Fig. 3). Assuming that there probably has been no significant mixing of clusters among different regions, the observed excess of clusters reveals that the cluster formation history in the outermost, eastern region of the SMC could have been influenced at some level by the galaxy's interaction with the LMC. Such an interaction (Nidever et al. 2013; Rezaei kh. et al. 2014) could have resulted in either by stripping mechanics (Bagheri, Cioni & Napiwotzki 2013; Noël et al. 2013), or in situ star formation processes (McCumber, Garnett & Dufour 2005; Ripepi et al. 2014), or a combination of both that caused the observed and modeled CFs to look different for ages younger than 1 Gyr.

7   CONCLUSIONS

In this paper, we have analysed CMDs of catalogued star clusters located in the outermost, eastern region of the SMC based on a YJK_s photometric data set obtained by the VISTA VMC collaboration. We focussed on tiles SMC 3_5, 4_5, 5_6, 6_5, and BRI 2_3, because they are among the first fully or mostly completed tiles in the eastern region of the SMC, which may also show evidence of the SMC's interaction history with the LMC. We obtained PSF photometry for stars in and projected towards 51 catalogued clusters of small angular size, typically ~ 12.2 pc in diameter, which represents a meaningful sample size for scientific studies.

We applied a field-star subtraction procedure to statistically clean the cluster CMDs from field-star contamination to disentangle cluster features from those associated with their surrounding fields. The technique we employed makes use of variable cells to reproduce the field CMDs as closely as possible. We found that nearly 30% (15 catalogued clusters) of the cluster sample investigated do not have cluster sequences in the cleaned CMDs an were therefore assumed to be possible non-genuine aggregates.

Based on matching theoretical isochrones in the VISTA system to the cleaned cluster CMDs, we obtained estimates of the cluster ages, assuming as initial guess for the cluster metalicity the value $Z = 0.003$. We took into account the SMC's distance modulus as well as the individual cluster colour excesses. The resulting cluster ages span the age range $7.0 \leqslant \log(t \text{ yr}^{-1}) \leqslant 9.8$. This cluster sample forms part of the cluster data base which will result from the VMC survey and which will be used to self-consistently study the overall cluster formation history of the Magellanic system. Fourteen clusters have previous age estimates based on the matching of isochrones to their CMDs. We studied seven of

these based on Washington CT_1 photometry, whereas the remaining clusters were studied by Glatt, Grebel & Koch (2010). Although the present cluster ages are in very good agreement with those resulting from analysis of Washington photometry, Glatt, Grebel & Koch (2010)'s ages are much younger, possibly because of the lack of cleaned CMDs and the shallower photometry used by these authors.

We complemented the properties of 80% of the catalogued clusters in this part of the SMC by increasing our sample by addition of previously determined cluster ages, taking care to adopt a homogeneous scale. Their spatial distribution seems to suggest that the oldest clusters – $\log(t \text{ yr}^{-1}) \leqslant 9.6$ – are in general located at greater distances from the galaxy's centre than their younger counterparts, $9.0 \leqslant \log(t \text{ yr}^{-1}) \leqslant 9.4$, which is in agreement with previous studies of star clusters and field stars. The latter showed that the greater their distances to the SMC centre, the older the clusters' ages are, with a non-negligible dispersion. Within the older cluster population, two excesses of clusters are seen, at $\log(t \text{ yr}^{-1}) \sim 9.0$–9.4 and $\log(t \text{ yr}^{-1}) \sim 9.6$–9.8, in very good agreement with the timing of enhanced episodes of cluster formation previously found throughout the galaxy.

We also found a trail of younger clusters that seems to follow the Wing/Bridge components. Such a long spatial sequence, which extends from the inner SMC disc, does not only harbour very young clusters – $\log(t \text{ yr}^{-1}) \sim 7.3$ – but it also includes some of intermediate ages, $\log(t \text{ yr}^{-1}) \sim 9.1$. Therefore, the Wing/Bridge structures seem to have existed at least during the last 1–2 Gyr, $\log(t \text{ yr}^{-1})$.

The observed and modeled CF, excluding tile BRI 2_3, are different. For ages in excess of $\log(t \text{ yr}^{-1}) \sim 9.4$, the model CF, obtained by assuming a cluster formation rate proportional to that of the field stars and a power-law mass distribution with a slope of $\alpha = -2$, is higher than the observed frequency, possibly because we did not take into account any cluster dissolution. For younger ages, the observed CF is – surprisingly – significantly higher than the model distribution, which may be partially owing to the fact that field-star formation activity is known to decrease from $\log(t \text{ yr}^{-1}) \sim 9.0$ until a burst-like formation event occurred at $\log(t \text{ yr}^{-1}) \sim 8.5$. Nevertheless, even though the model CF requires additional refinements, if we assume that there probably has been no significant mixing of clusters among different regions, the observed excess of clusters reveals that the cluster formation history in the outermost, eastern region of the SMC could have been influenced at some level by the galaxy's interaction history with the LMC.

REFERENCES

Arnaboldi M. et al., 2013, The Messenger, 154, 18

Bagheri G., Cioni M.-R. L., Napiwotzki R., 2013, A&A, 551, A78

Baumgardt H., Parmentier G., Anders P., Grebel E. K., 2013, MNRAS, 430, 676

Bekki K., Chiba M., 2007, MNRAS, 381, L16

Bertin E., Mellier Y., Radovich M., Missonnier G., Didelon P., Morin B., 2002, in Astronomical Society of the Pacific Conference Series, Vol. 281, Astronomical Data Analysis Software and Systems XI, D. A. Bohlender, D. Durand, & T. H. Handley, ed., pp. 228–+

Bica E., Bonatto C., Dutra C. M., Santos J. F. C., 2008, MNRAS, 389, 678

Bica E., Santos, Jr. J. F. C., Schmidt A. A., 2008, MNRAS, 391, 915

Bratsolis E., Kontizas M., Bellas-Velidis I., 2004, A&A, 423, 919

Bressan A., Marigo P., Girardi L., Salasnich B., Dal Cero C., Rubele S., Nanni A., 2012, MNRAS, 427, 127

Cardelli J. A., Clayton G. C., Mathis J. S., 1989, ApJ, 345, 245

Carrera R., Gallart C., Aparicio A., Costa E., Méndez R. A., Noël N. E. D., 2008, AJ, 136, 1039

Cignoni M., Cole A. A., Tosi M., Gallagher J. S., Sabbi E., Anderson J., Grebel E. K., Nota A., 2013, ApJ, 775, 83

Cioni M.-R. L. et al., 2011, A&A, 527, A116

Cross N. J. G. et al., 2012, A&A, 548, A119

Crowl H. H., Sarajedini A., Piatti A. E., Geisler D., Bica E., Clariá J. J., Santos, Jr. J. F. C., 2001, AJ, 122, 220

Da Costa G. S., Hatzidimitriou D., 1998, AJ, 115, 1934

de Grijs R., Goodwin S. P., 2008, MNRAS, 383, 1000

de Grijs R., Goodwin S. P., Anders P., 2013, MNRAS, 436, 136

Dolphin A. E., Walker A. R., Hodge P. W., Mateo M., Olszewski E. W., Schommer R. A., Suntzeff N. B., 2001, ApJ, 562, 303

Dutra C. M., Bica E., Clariá J. J., Piatti A. E., Ahumada A. V., 2001, A&A, 371, 895

Gao J., Jiang B. W., Li A., Xue M. Y., 2013, ApJ, 776, 7

Geisler D., Sarajedini A., 1999, AJ, 117, 308

Glatt K. et al., 2008, AJ, 135, 1106

—, 2011, AJ, 142, 36

Glatt K., Grebel E. K., Koch A., 2010, A&A, 517, A50

Gouliermis D. A., Quanz S. P., Henning T., 2007, ApJ, 665, 306

Harris J., 2007, ApJ, 658, 345

Harris J., Zaritsky D., 2001, ApJS, 136, 25

—, 2004, AJ, 127, 1531

Haschke R., Grebel E. K., Duffau S., 2011, AJ, 141, 158

Irwin M. J. et al., 2004, in Society of Photo-Optical Instrumentation Engineers (SPIE) Conference Series, Vol. 5493, Optimizing Scientific Return for Astronomy through Information Technologies, Quinn P. J., Bridger A., eds., pp. 411–422

Lada C. J., Lada E. A., 2003, ARA&A, 41, 57

Lewis J. R., Irwin M., Bunclark P., 2010, in Astronomical Society of the Pacific Conference Series, Vol. 434, Astronomical Data Analysis Software and Systems XIX, Mizumoto Y., Morita K.-I., Ohishi M., eds., p. 91

Li C. et al., 2014, ApJ, 790, 35

McCumber M. P., Garnett D. R., Dufour R. J., 2005, AJ, 130, 1083

Mighell K. J., Sarajedini A., French R. S., 1998, AJ, 116, 2395

Moretti M. I. et al., 2014, MNRAS, 437, 2702

Nidever D. L., Monachesi A., Bell E. F., Majewski S. R., Muñoz R. R., Beaton R. L., 2013, ApJ, 779, 145

Noël N. E. D., Aparicio A., Gallart C., Hidalgo S. L., Costa E., Méndez R. A., 2009, ApJ, 705, 1260

Noël N. E. D., Conn B. C., Carrera R., Read J. I., Rix H.-W., Dolphin A., 2013, ApJ, 768, 109

Parisi M. C. et al., 2014, AJ, 147, 71

Piatti A. E., 2011a, MNRAS, 416, L89

—, 2011b, MNRAS, 418, L69

—, 2012a, ApJ, 756, L32

—, 2012b, MNRAS, 422, 1109

—, 2014a, MNRAS, 440, 3091

—, 2014b, MNRAS, 437, 1646

Piatti A. E., Bica E., 2012, MNRAS, 425, 3085

Piatti A. E., Clariá J. J., Bica E., Geisler D., Ahumada A. V., Girardi L., 2011, MNRAS, 417, 1559

Piatti A. E., Geisler D., 2013, AJ, 145, 17

Piatti A. E., Geisler D., Sarajedini A., Gallart C., Wischnjewsky M., 2008, MNRAS, 389, 429

Piatti A. E. et al., 2014, ArXiv e-prints

Piatti A. E., Sarajedini A., Geisler D., Clark D., Seguel J., 2007a, MNRAS, 377, 300

Piatti A. E., Sarajedini A., Geisler D., Gallart C., Wischnjewsky M., 2007b, MNRAS, 382, 1203

—, 2007c, MNRAS, 381, L84

Rezaei kh. S., Javadi A., Khosroshahi H., van Loon J. T., 2014, ArXiv e-prints

Ripepi V. et al., 2014, MNRAS, 442, 1897

—, 2012, MNRAS, 424, 1807

Rubele S. et al., 2015, ArXiv e-prints

—, 2012, A&A, 537, A106

Sabbi E. et al., 2009, ApJ, 703, 721

Skowron D. M. et al., 2014, ArXiv e-prints

Stetson P. B., Davis L. E., Crabtree D. R., 1990, in Astronomical Society of the Pacific Conference Series, Vol. 8, CCDs in astronomy, Jacoby G. H., ed., pp. 289–304

Tatton B. L. et al., 2013, A&A, 554, A33

Testor G., Lemaire J. L., Heydari-Malayeri M., Kristensen L. E., Diana S., Field D., 2010, A&A, 510, A95

Udalski A., 2003, Acta Astron., 53, 291

Zaritsky D., Harris J., Thompson I. B., Grebel E. K., Massey P., 2002, AJ, 123, 855

10 *A. E. Piatti et al.*

Table 1. VMC tile information.

Tile ID	RA (J2000) (°)	Dec (J2000) (°)	Completion in the K_s filter	$mag_{0.1}$ Y	J	K_s	50% Completeness level Y	J	K_s
SMC 3_5	21.9762	−74.0018	100%	21.73	21.70	20.62	22.24	22.09	21.02
SMC 4_5	21.2959	−72.9339	100%	22.09	21.72	20.65	22.43	22.15	21.08
SMC 5_6	25.4401	−71.5879	92%	22.02	21.70	20.61	22.52	22.12	20.98
SMC 6_5	20.4138	−70.7601	100%	22.07	21.58	20.59	22.48	22.20	20.93
BRI 2_3	33.6941	−74.0132	92%	21.79	21.62	20.68	21.93	21.71	20.96

Table 3. Fundamental parameters of additional SMC clusters.

Name	$\log(t \, yr^{-1})$	[Fe/H]	Reference
BS196	9.70±0.05	−1.7±0.1	1
HW66	9.60±0.10	−1.3±0.2	2
HW79	9.70±0.10	−1.3±0.2	2
HW86	**9.15**±0.10	**−0.65**±0.20	2, **6**
L100	9.30±0.10	−0.7±0.2	2
L106	9.20±0.15	−0.7±0.2	2
L108	**9.30**±0.10	**−0.9**±0.2	2, **6**
L111	**9.15**±0.10	**−0.75**±0.20	2, **6**
L112	**9.75**±0.10	−1.1±0.2	2, **6**
L113	**9.70**±0.10	−1.17±0.12	3, 4, **6**
L114	8.15±0.15	−0.7±0.2	5
L115	8.05±0.10	−0.7±0.2	5

References: (1) Bica, Santos & Schmidt (2008); (2) Piatti et al. (2011); (3) Piatti et al. (2007c); (4) Da Costa & Hatzidimitriou (1998); (5) Piatti et al. (2007b); (6) **Parisi et al. (2014).**

Table 2. Fundamental parameters of the SMC clusters studied.

Name	RA (°)	Dec (°)	Diameter (′)	$E(B-V)$ (mag)	$\log(t \, \mathrm{yr}^{-1})$	Z	Comments
				SMC 3_5			
GKH51*	022.277	−73.5635	0.30	0.08	...	...	possible non-cluster (1)
B165	022.711	−73.434	0.45	0.08	...	...	possible non-cluster
B166	022.975	−73.910	0.60	0.08	8.3	0.003	
L109	023.306	−74.167	0.90	0.07	9.6	0.003	9.55±0.10 (2), **9.50±0.05 (7)**
SGDH-cluster A	022.308	−73.532	0.40	0.06	...	...	possible non-cluster (1)
B164	022.369	−73.533	0.60	0.08	8.5	0.003	
GKH54/57*	022.400	−73.551	0.10	0.08	...	...	possible non-cluster (1)
GKH29*	022.400	−73.558	0.10	0.08	...	...	possible non-cluster (1)
GKH24*	022.412	−73.555	0.05	0.08	...	...	not resolved (1)
GKH22	022.421	−73.563	0.40	0.08	...	...	not resolved (1)
HW75	019.372	−73.570	0.90	0.06	8.3	0.003	8.20±0.40 (6)
B155	020.099	−74.004	0.50	0.04	8.7	0.003	
				SMC 4_5			
HW74	019.194	−73.1605	0.55	>0.06	8.8	0.003	7.50±0.20 (6)
B156	019.891	−73.0967	0.65	0.06	...	...	possible non-cluster; 7.50±0.20 (6)
HW72	018.923	−73.167	0.50	0.06	8.7	0.003	8.10±0.20 (6)
K68,L98	018.890	−72.624	0.70	0.05	8.7	0.003	8.20±0.20 (6)
B162	020.963	−73.440	0.55	0.06	7.3	0.003	
H86-211	021.191	−73.425	0.50	0.06	...	...	possible non-cluster
H86-212	021.313	−73.501	0.60	0.06	...	...	possible non-cluster
BS282	021.375	−73.3895	0.40	0.06	...	...	possible non-cluster
HW77	020.044	−72.622	1.40	0.06	9.15	0.003	
HW78	020.335	−73.094	0.45	0.06	...	...	possible non-cluster
HW81	021.042	−73.154	1.00	>0.3	7.0	0.003	
BS176	021.063	−73.1685	0.35	0.06	8.3	0.003	
L110	023.608	−72.874	2.40	0.06	9.8	0.003	9.80±0.10 (3), **9.90±0.10 (7)**
H86-213	023.673	−73.2755	0.40	0.07	8.8	0.003	
HW82	021.114	−73.172	0.70	0.06	7.8	0.003	
HW80	020.858	−73.224	0.70	0.06	...	...	possible non-cluster
BS187	022.754	−72.851	0.60	0.04	9.3	0.003	
Sk158	018.971	−73.319	0.70	0.06	7.3	0.003	
Sk157	018.965	−73.347	0.60	0.06	7.2	0.003	
				SMC 5_6			
BS188	023.796	−71.737	0.80	0.07	9.2	0.003	
HW84	025.431	−71.162	1.20	0.07	9.25	0.003	9.20±0.10 (2)
HW85	025.615	−71.2795	0.70	0.07	9.4	0.003	9.30±0.10 (2)
BS189	025.777	−71.452	1.20	2.80	7.3	0.003	
BS190	025.963	−71.747	1.20	0.50	8.5	0.003	
				SMC 6_5			
HW73	019.105	−71.327	0.80	0.05	8.3	0.003	8.15±0.20 (6)
L95	018.690	−71.348	0.50	0.05	8.4	0.003	8.30±0.20 (6)
H86-197	018.882	−71.176	0.50	0.06	9.3	0.006	9.10±0.10 (5)
HW67	018.259	−70.964	0.95	0.06	9.2	0.003	9.20±0.10 (4)
BS173	021.017	−70.327	1.00	0.06	...	...	possible non-cluster
B168	021.678	−70.785	0.50	0.06	9.6	0.003	
IC1708	021.233	−71.185	1.00	0.07	9.1	0.003	9.10±0.10 (2)
				BRI 2_3			
BS226	031.425	−74.381	0.40	...	...	...	not recognized
BS229	031.952	−74.4425	0.50	0.08	7.3	0.003	
BS232	032.340	−74.026	0.50	0.08	...	...	possible non-cluster
BS233	032.658	−74.156	1.20	0.15	7.3	0.003	
BS235	032.962	−74.119	0.60	0.09	...	...	possible non-cluster
BS239	033.651	−73.985	1.20	0.11	8.5	0.003	
BSBD4	033.667	−74.358	0.60	0.08	9.1	0.003	
BS240	033.717	−73.953	0.35	0.09	...	...	possible non-cluster

1
2
3
4
5
6
7
8
9
10
11
12
13
14
15
16
17
18
19
20
21
22
23
24
25
26
27
28
29
30
31
32
33
34
35
36
37
38
39
40
41
42
43
44
45
46
47
48
49
50
51
52
53
54
55
56
57
58
59
60

12   *A. E. Piatti et al.*

Table 2. continued.

* In Table 3 of Bica et al. (2008) the acronym GHK appears instead of GKH (see their table 1).

References: (1) Gouliermis, Quanz & Henning (2007); (2) Piatti et al. (2011, CT_1 data); (3) Piatti et al. (2007c, CT_1 data); (4) Piatti (2011b, CT_1 data); (5) Piatti & Bica (2012, CT_1 data); (6) Glatt, Grebel & Koch (2010); **(7) Parisi et al. (2014).**

1
2
3
4
5
6
7
8
9
10
11
12
13
14
15
16
17
18
19
20
21
22
23
24
25
26
27
28
29
30
31
32
33
34
35
36
37
38
39
40
41
42
43
44
45
46
47
48
49
50
51
52
53
54
55
56
57
58
59
60
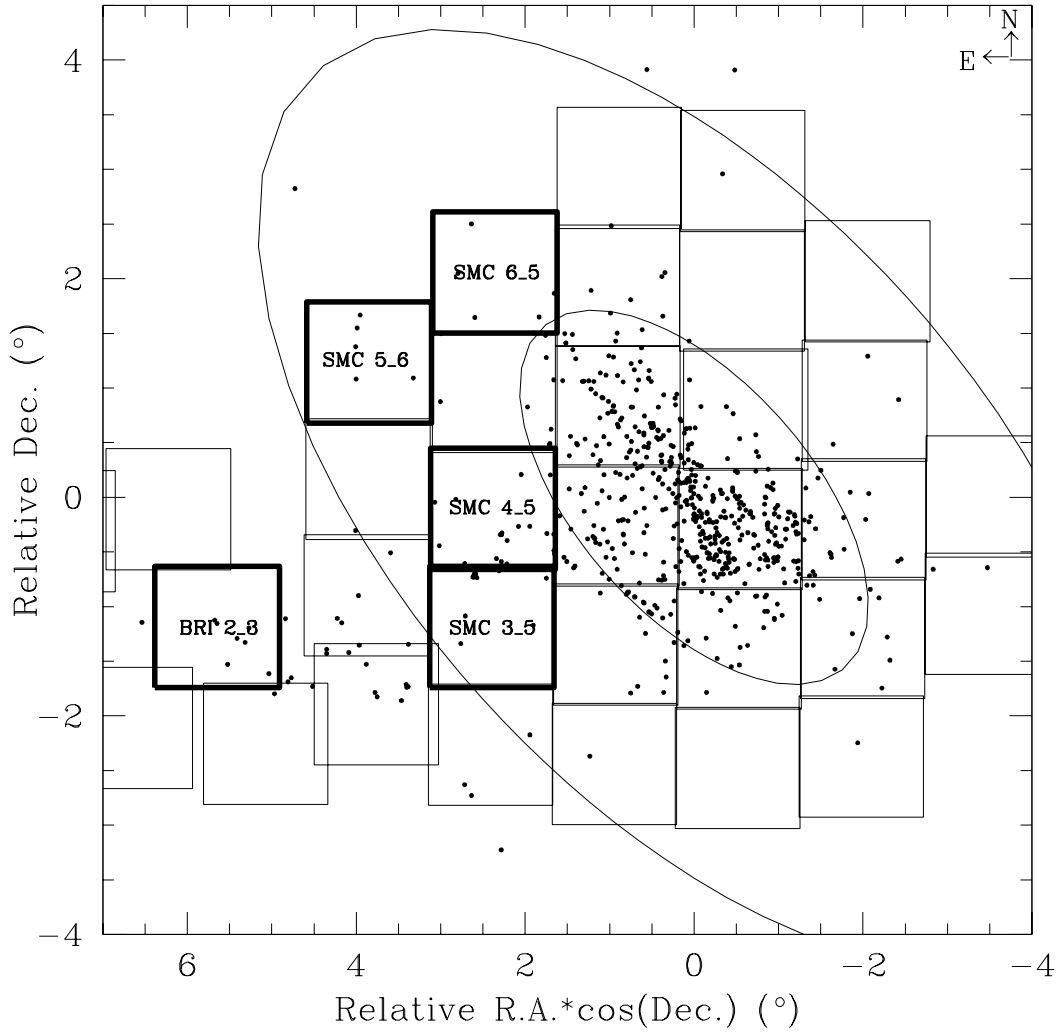
Figure 1. Spatial distribution of VISTA tiles across the SMC and the western Bridge regions. The distribution of SMC clusters (dots) as well as ellipses with semimajor axes of 2.4° and 6° are overplotted. The SMC tiles studied here have been labelled and highlighted with thick lines.
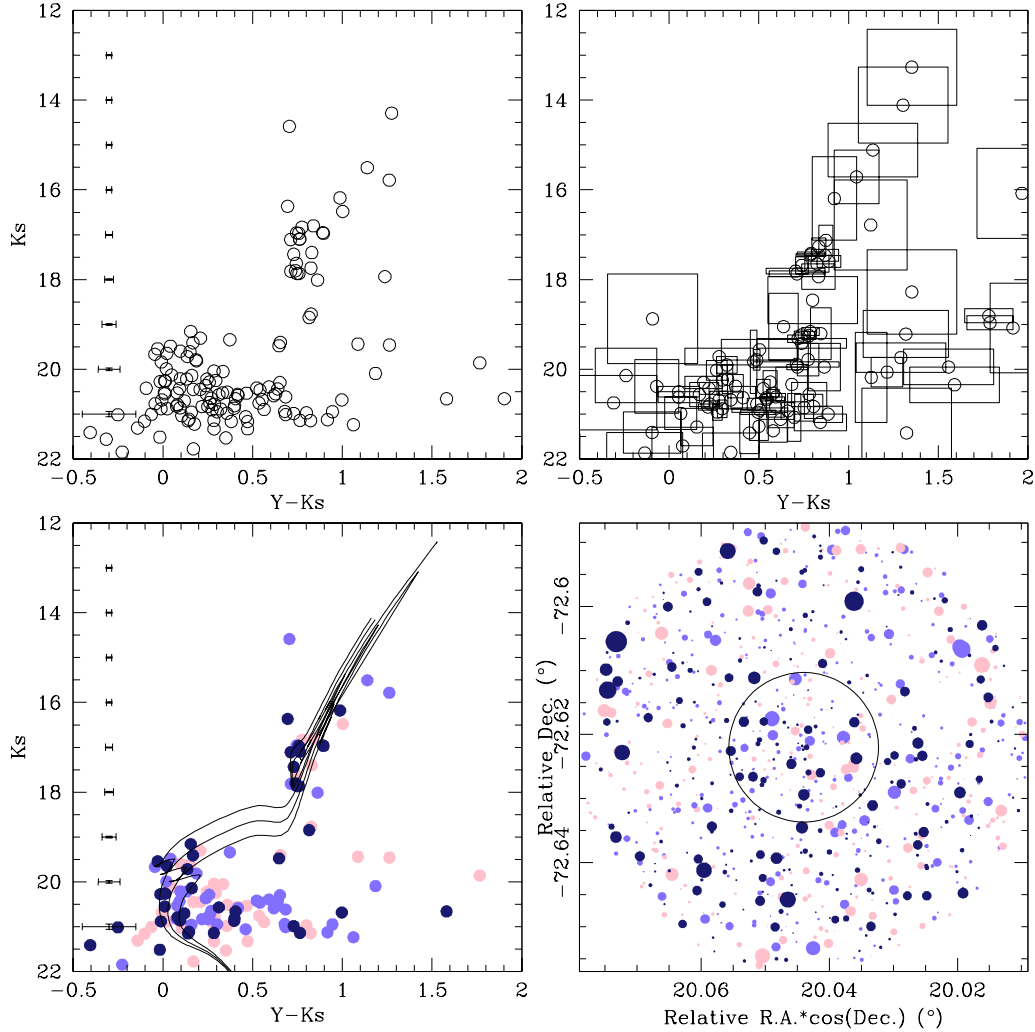
14   *A. E. Piatti et al.*

Figure 2. CMDs for stars in the field of HW 77 of tile SMC 4_5: the observed CMD composed of the stars distributed within the cluster radius (top left-hand panel); a field CMD for an annulus -outer and inner radii equal to 3.163 and 3.0 times the cluster radius- centred on the cluster (top right-hand panel); the cleaned cluster CMD (bottom left). We overplotted boxes for each star in the field CMD to be used in the cluster CMD field decontamination (see Section 4 for details). Colour-scaled symbols represent stars that statistically belong to the field ($P \leqslant 25\%$, pink), stars that might belong to either the field or the cluster ($P = 50\%$, light blue), and stars that predominantly populate the cluster region ($P \geqslant 75\%$, dark blue). Three isochrones from Bressan et al. (2012) for $\log(t\,\mathrm{yr}^{-1})$, $\log(t\,\mathrm{yr}^{-1}) \pm 0.1$, and the metallicity values listed in Table 2 are also superimposed. The schematic diagram centred on the cluster for a circle of radius three times the cluster radius is shown in the bottom right-hand panel. The black circle represents the adopted cluster radius. Symbols are as in the bottom left-hand panel, with sizes proportional to the stellar brightnesses. North is up; east is to the left.
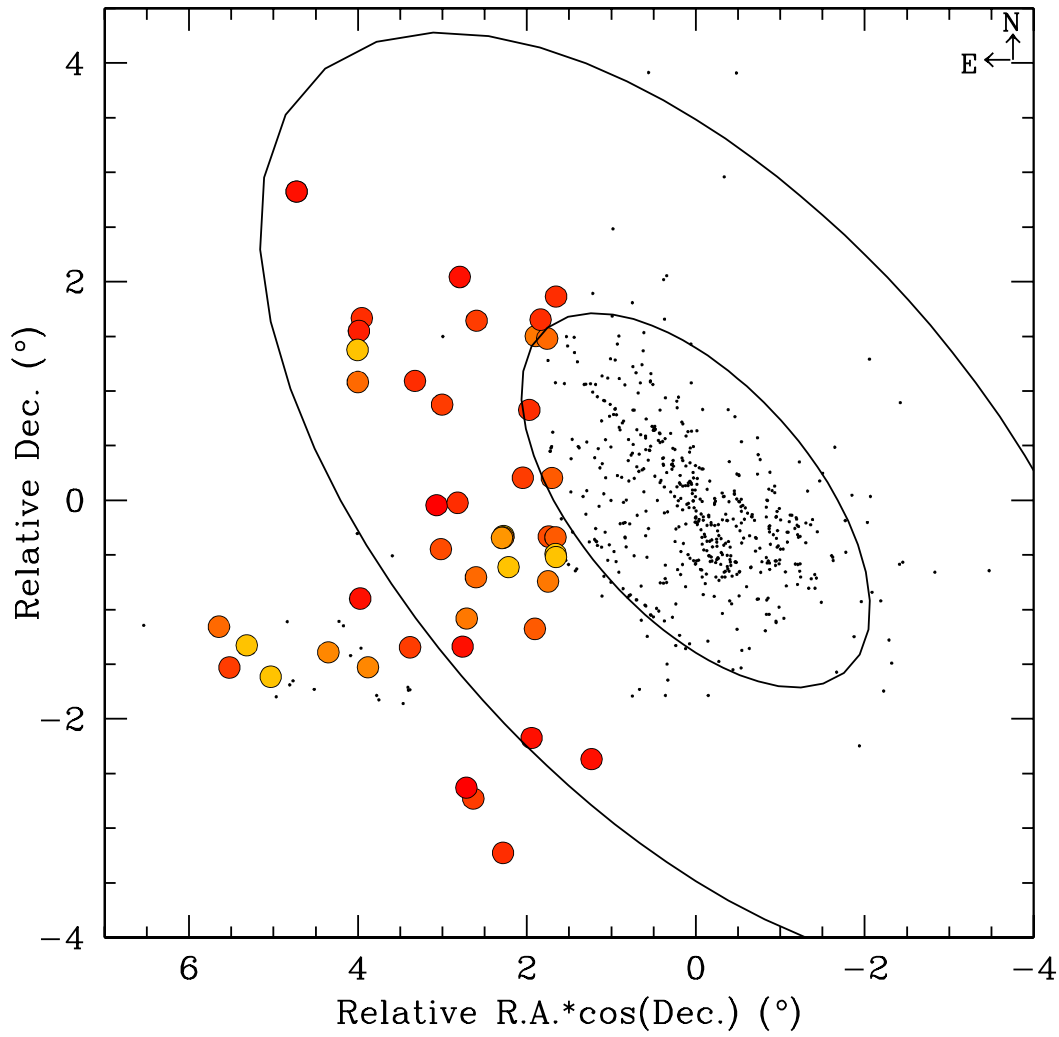
Figure 3. Spatial distribution of the enlarged SMC cluster sample (solid circles), where darker solid circles correspond to older cluster ages. Catalogued clusters (dots) and ellipses with semimajor axes of 2.4° and 6° are overplotted.
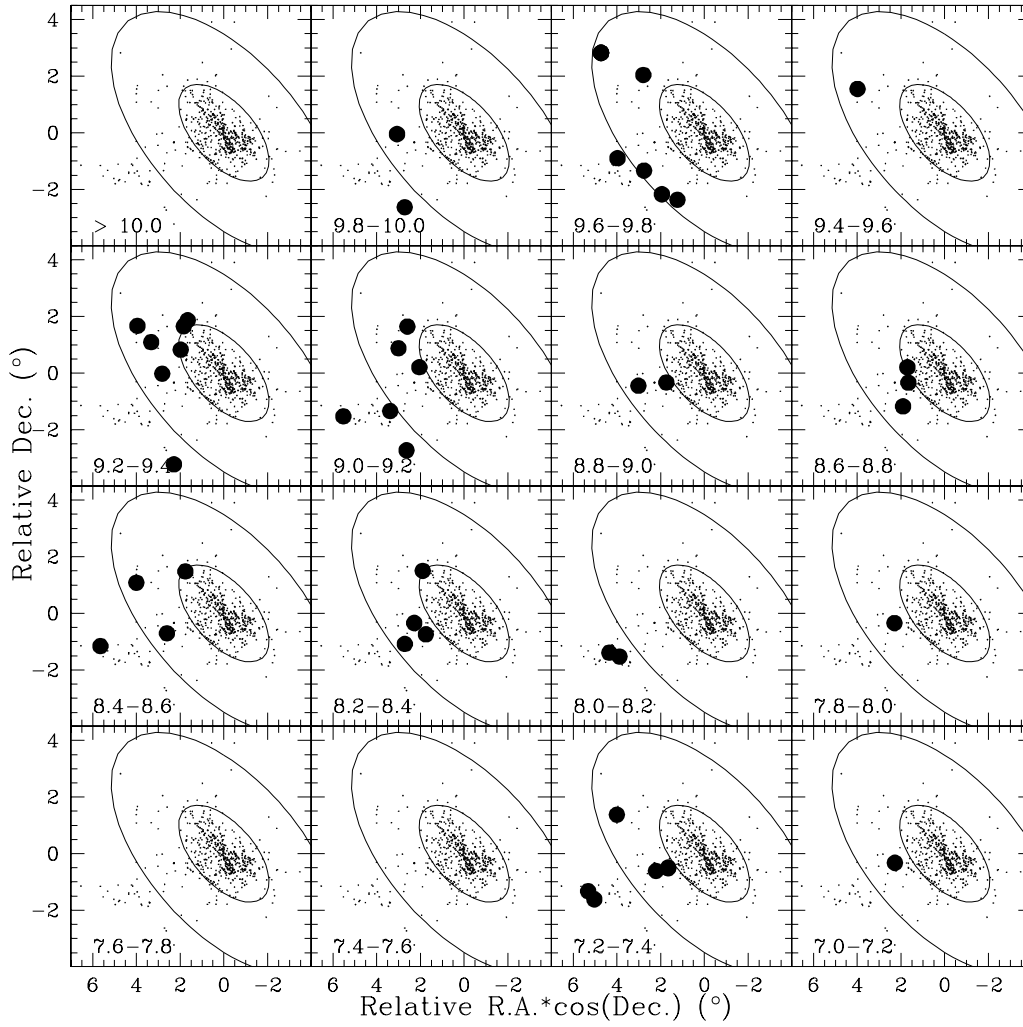
16   *A. E. Piatti et al.*

Figure 4. As Fig. 3, but for different $\log(t \text{ yr}^{-1})$ intervals, as labelled in each panel; the lower **age** limit **is** included in the respective interval.

1
2
3
4
5
6
7
8
9
10
11
12
13
14
15
16
17
18
19
20
21
22
23
24
25
26
27
28
29
30
31
32
33
34
35
36
37
38
39
40
41
42
43
44
45
46
47
48
49
50
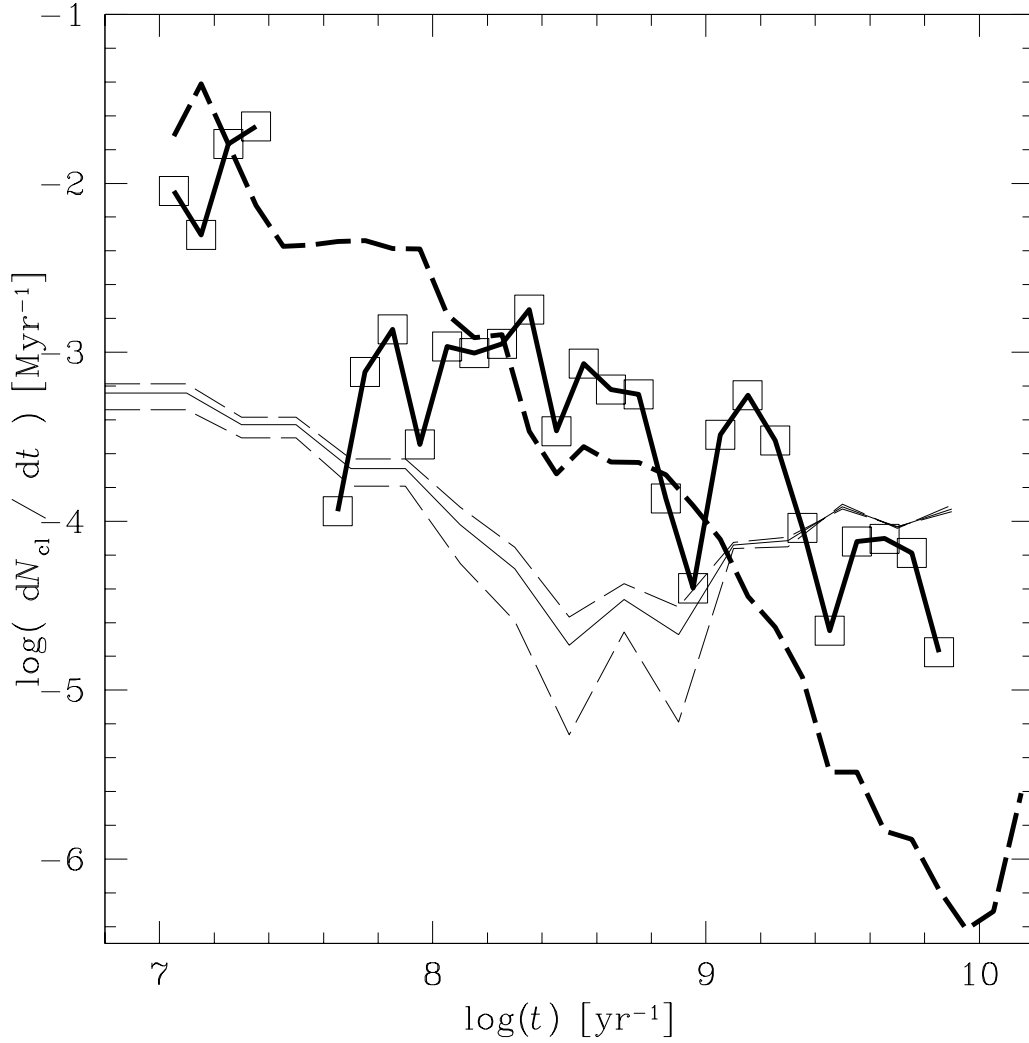51
52
53
54
55
56
57
58
59
60

Figure 5. Comparison of the observed CFs (open boxes connected by a thick solid line) and the theoretical CF (thin solid line). The error curves for the latter are shown as thin dashed lines. The CF constructed on the basis of the cluster age determinations of de Grijs & Goodwin (2008) is overplotted with a thick dashed line.